

FAR-INFRARED AND SUBMILLIMETER OBSERVATIONS AND PHYSICAL MODELS OF THE REFLECTION NEBULA CEDERBLAD 201

CISKA KEMPER¹

Leiden Observatory, P.O. Box 9513, 2300 RA, Leiden, Netherlands

MARCO SPAANS²

Harvard-Smithsonian Center for Astrophysics, Cambridge, MA 02138

DAVID J. JANSEN

Leiden Observatory, P.O. Box 9513, 2300 RA, Leiden, Netherlands

MICHEL R. HOGERHEIJDE³

Leiden Observatory, P.O. Box 9513, 2300 RA, Leiden, Netherlands

EWINE F. VAN DISHOECK

Leiden Observatory, P.O. Box 9513, 2300 RA, Leiden, Netherlands

AND

ALEXANDER G. G. M. TIELENS

Kapteyn Institute, P.O. Box 800, 9700 AV, Groningen, Netherlands

Received 1998 August 7; accepted 1998 November 24

ABSTRACT

Infrared Space Observatory (ISO) [C II] 158 μm , [O I] 63 μm , and H₂ 9 and 17 μm observations are presented of the reflection nebula Ced 201, which is a photon-dominated region (PDR) illuminated by a B9.5 star with a color temperature of 10,000 K (a cool PDR). In combination with ground-based [C I] 609 μm , CO, ¹³CO, CS, and HCO⁺ data, the carbon budget and physical structure of the reflection nebula are constrained. The obtained data set is the first one to contain all important cooling lines of a cool PDR and allows a comparison to be made with classical PDRs. To this effect one- and three-dimensional PDR models are presented that incorporate the physical characteristics of the source and are aimed at understanding the dominant heating processes of the cloud. The contribution of very small grains to the photoelectric heating rate is estimated from these models and is used to constrain the total abundance of polycyclic aromatic hydrocarbons and small grains. Observations of the pure rotational H₂ lines with *ISO*, in particular the S(3) line, indicate the presence of a small amount of very warm ~ 330 K molecular gas. This gas cannot be accommodated by the presented models.

Subject headings: dust, extinction — ISM: individual (Cederblad 201) — molecular processes — reflection nebulae

1. INTRODUCTION

A major problem concerning the interstellar medium and circumstellar regions remains the identification of the dominant gas heating source. The best current model is photoelectric emission by dust grains following irradiation by ultraviolet photons. The ejected electrons carry an excess kinetic energy of a few electron volts, which is transferred to the gas by elastic collisions with H and H₂. The efficiency of this photoelectric heating for various densities and illuminating radiation fields has been the subject of many investigations (Hollenbach & Tielens 1997; Spaans et al. 1994 and references therein). Bakes & Tielens (1994) presented calculations for the contribution of very small grains (VSGs) and large molecules like polycyclic hydrocarbons (PAHs) to the total heating rate. To establish a firm theoretical basis for interstellar heating, one therefore has to constrain the abundance of these putative species.

In this work, *Infrared Space Observatory (ISO)* and ground-based observations are presented of the reflection

nebula Ced 201. Since the illuminating star has an effective temperature of 10,000 K, Ced 201 qualifies as a cool photon-dominated region (PDR). That is, the relatively soft impinging radiation field decreases the photoelectric heating rate, leading to cooler temperatures. Furthermore, the resulting photoelectric heating rate has larger contributions from grain species with low ionization potentials and negative (or small positive) charges (Bakes & Tielens 1994). Ced 201 is thus ideally suited to investigate the role of PAHs in the photoelectric heating process (Spaans et al. 1994).

Most PDR models to date are constructed for classical PDRs, i.e., PDRs illuminated by O or early-type B stars. The aim of this study is to use a complete set of atomic and molecular diagnostics to constrain the total cooling, the density, the extinction, and the illuminating radiation field of a cool PDR. If the physical and chemical structure of the source can be determined consistent with the observations through PDR models, then it is possible to estimate the contribution of VSGs and PAHs to the total photoelectric heating rate. *ISO* offers a new opportunity to probe the physics and chemistry of PDRs by observations of the major cooling lines [C II] 158 μm and [O I] 63 μm with the Long Wavelength Spectrometer (LWS) and searches for the pure rotational lines of H₂ with the Short Wavelength Spectrometer (SWS). The latter lines provide important

¹ Currently at the University of Amsterdam, Kruislaan 403, Amsterdam, The Netherlands.

² Hubble Fellow.

³ Currently at the University of California in Berkeley, 601 Campbell Hall, CA 94720.

constraints on the amount of warm gas in the source, which may not be explained by current models (Timmerman et al. 1996). Searches of these LWS and SWS lines in weak, extended sources such as discussed here have not been previously possible with airborne observatories.

2. OBSERVATIONS

Cederblad 201 is associated with BD +69°1231, a main-sequence star of spectral type B9.5 and an effective temperature of 10,000 K. The source is located toward $\alpha = 22:12:14$ and $\delta = 70:00:11$ (epoch 1950) and lies at a distance of approximately 420 pc (Casey 1991). In this study an extended set of observations of Ced 201 is presented. The source is mapped around the offset position in $^{12}\text{CO } 2 \rightarrow 1$ and $3 \rightarrow 2$ line emission. Additional observations of line transitions of other species are performed at the maximum of the $^{12}\text{CO } 2 \rightarrow 1$ emission. The most important observations are obtained with the James Clerk Maxwell Telescope⁴ (JCMT) and *ISO* and are presented in the following sections after the NRAO results.

2.1. NRAO Observations

Single-dish observations of the $\text{HCO}^+ 1-0$ and $\text{CS } 2-1$ lines were made in 1996 June with the NRAO 12 m telescope on Kitt Peak.⁵ The adopted receiver was the 3 mm

SIS dual channel mixer. For the back end, the Hybrid Spectrometer was placed in dual channel mode with a resolution of 47.9 KHz (0.16 km s^{-1}). The beamwidth is $63''$ FWHM, and the main beam efficiency $\eta_{\text{MB}} = 0.86$. Pointing is accurate to $10''$ in azimuth and $5''$ in elevation. A weak detection of $\text{HCO}^+ 1 \rightarrow 0$ was found, but the $\text{CS } 2 \rightarrow 1$ line was not detected (see Table 2).

2.2. JCMT Observations

Observations of the $^{12}\text{CO } 2 \rightarrow 1$ and $3 \rightarrow 2$, $^{13}\text{CO } 2 \rightarrow 1$ and $3 \rightarrow 2$, $\text{C}^{18}\text{O } 2 \rightarrow 1$, $\text{HCO}^+ 3 \rightarrow 2$, and $[\text{C I}]$ (492 GHz/609 μm) line transitions were performed in three different wavelength bands. The front-end receivers, the telescope beam sizes, and the efficiencies at the various frequencies are shown in Table 1. The main beam efficiencies η_{MB} were determined from observations of planets by the JCMT staff. All observations were obtained in the 125 MHz configuration, corresponding to a channel width of 0.078 MHz. For these high-resolution spectra, the Digital Autocorrelating Spectrometer at the back end of the receiver was used. All observations were made in position-switching mode, using an offset of 30', 45', or 90' in azimuth. In this mode, the telescope integrates at the source position for 30 s and then switches to an emission-free position on the sky. The difference between these two signals yields the actual source contribution, assuming that the atmospheric conditions do not vary significantly on the timescale of a minute. Low-order polynomial baseline fits were adopted in the reduction.

Table 2 shows an overview of the line transitions observed at the offset position ($0'', 0''$), and Figure 1 shows the $^{12}\text{CO } 2 \rightarrow 1$ and $3 \rightarrow 2$ line emission maps. Most line profiles can be fitted with a Gaussian at $V_{\text{LSR}} = -4.9 \text{ km s}^{-1}$, although in several spectra a smaller peak at $V_{\text{LSR}} = -5.9 \text{ km s}^{-1}$ also occurs. This study will focus on the emission at $V_{\text{LSR}} = -4.9 \text{ km s}^{-1}$. For Ced 201, the ^{12}CO line profiles do not exhibit the characteristic double-peaked shape of self-absorption, except for a few offset positions, located near the edge of the mapped regions, which are not associated with the central PDR. Therefore, it can be concluded that the illuminating star is located between the observer and the central cloud, heating the gas from the outside.

TABLE 1
TECHNICAL DETAILS OF THE JCMT

Receiver	Frequency (GHz)	η_{MB}	θ_{beam} (arcsec)
RxA2	230	0.69 ± 0.03	21 ± 2
RxB3i	345	0.58 ± 0.02	14.1 ± 0.5
RxC2	460	0.52 ± 0.05	10.9 ± 0.5

⁴ The James Clerk Maxwell Telescope is operated by the Joint Astronomy Centre, Hilo (Hawaii), on behalf of the UK Particle Physics and Astronomy Research Council, the Netherlands Organization for Scientific Research (NWO), and the National Research Council of Canada.

⁵ The National Radio Astronomical Observatory is operated by Associated Universities, Inc., under contract with the US National Science Foundation.

TABLE 2
SUBMILLIMETER OBSERVATIONS OF CED 201

Line	I (K km s ⁻¹)	$T_{\text{peak}}^{\text{a}}$ (K)	ΔV (km s ⁻¹)	V_{LSR} (km s ⁻¹)	rms ^b (K)
$\text{HCO}^+ 1 \rightarrow 0$	1	0.15	0.85	-5	0.03
$\text{CS } 2 \rightarrow 1$	<0.03	0.03
$^{12}\text{CO } 2 \rightarrow 1$	21.3	23.2	0.86	-4.9	0.53
	7.6	6.8	1.1	-5.9	0.53
$^{12}\text{CO } 3 \rightarrow 2$	25.3	33.1	0.72	-4.9	0.94
	7.8	6.8	1.1	-5.9	0.94
$^{13}\text{CO } 2 \rightarrow 1$	5.4	6.9	0.73	-4.9	0.71
	1.7	1.5	1.1	-5.9	0.71
$^{13}\text{CO } 3 \rightarrow 2$	3.9	5.5	0.66	-4.9	1.0
	...	<0.64	...	-5.9	0.64
$\text{C}^{18}\text{O } 2 \rightarrow 1$	<0.09	0.09
$\text{HCO}^+ 3 \rightarrow 2$	<0.08	0.08
$[\text{C I}]$ (609 μm)	<1.3	1.3

^a In case of no detection, the upper limit, obtained by Hanning smoothing once, is shown.

^b Measured per channel of 0.078 MHz.

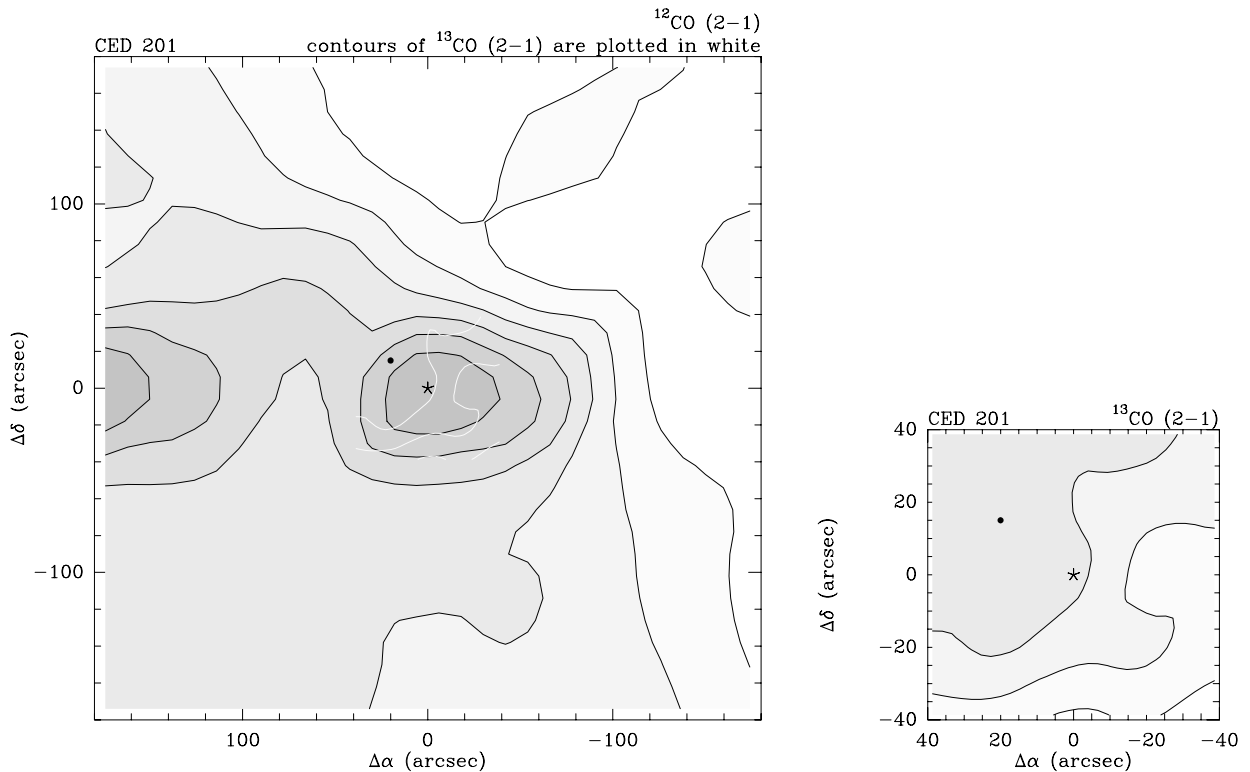


FIG. 1.—Contour plot of Ced 201. In the left-hand panel the integrated line intensities with spacings of 60" of the ^{12}CO 2 → 1 transition are shown. The contours represent values of 0.6, 5, 10, 15, 20, and 25 K km s^{-1} . The right-hand panel presents the integrated line intensities of the ^{13}CO 2 → 1 line with spacings of 20". The contour values correspond to 2, 4, and 6 K km s^{-1} . The ^{13}CO 2 → 1 emission is also indicated in white in the left-hand panel.

2.3. ISO Observations

Observations of the fine-structure lines of neutral oxygen [O I] and ionized carbon [C II], as well as the pure rotational transitions of molecular hydrogen, have been performed by *ISO*. The LWS (Clegg et al. 1996) AOT02 grating mode was used to obtain spectra of the [O I] (63 μm), [O I] (145 μm), and [C II] (158 μm) fine-structure lines, whereas the H_2 S(1) and S(3) transitions were obtained using the SWS (de Graauw et al. 1996) AOT02 grating mode. The [C II] and H_2 observations show unresolved line profiles, while the [O I] spectra only yield upper limits, as summarized in Table 3. The reduction was performed with the LWS version 6.0 pipeline software and the SWS reduction package (W.-F. Thi 1997, private communication). The detection of the S(1) and S(3) pure rotation H_2 lines indicates warm ($T > 200$ K) gas. This result will be further explored through the physical models constructed below.

2.4. Comparison with Other Lines of Sight

Before discussing the construction of specific models for Ced 201, it is good to compare the observed [C II] 158 μm line intensity, which accounts for 50% of the total cooling

rate in moderate-density PDRs ($n_{\text{H}} < 10^4 \text{ cm}^{-3}$), with other lines of sight. The above value translates into $2 \times 10^{-5} \text{ ergs s}^{-1} \text{ cm}^{-2} \text{ sr}^{-1}$, which should be compared with 2.2×10^{-3} for W3 (Boreiko, Betz, & Zmuidzinas 1993) and 4.6×10^{-4} for S140 (Minchin et al. 1994). Because the [C II] flux scales roughly linear with the impinging UV flux in this regime, care should be taken in comparing these numbers. It will be shown below that the strength of the incident radiation in interstellar units is $G_0 = 200$ for Ced 201, roughly equal to the S140 value, whereas W3 is characterized by $G_0 \sim 5 \times 10^3$. With these numbers one finds that the Ced 201 [C II] line is underluminous. The remaining difference between the various lines of sight, and the topic of this work, is the shape of illuminating radiation field.

Since the effective temperature of the illuminating star is 10,000 K, whereas it is $\sim 30,000$ K for S140 and W3, one would expect Ced 201 to be well described by cool PDR models. These exhibit a much smaller [C II]/CO ratio for the higher rotational levels of CO, $J \geq 3$ (Spaans et al. 1994). The reasons are that (1) the soft radiation field causes lower temperatures and hence smaller collisional excitation rates and (2) the abundance ratio C^+/CO is much larger in a soft UV field since C ionization and CO dissociation occur in the 912–1110 \AA wavelength range. Indeed, the [C II] line flux is not only small in Ced 201, which by itself may be due to abundance, temperature, and (column) density effects, it is also small compared with the observed CO 3–2 line with a ratio of about 100. This is roughly an order of magnitude smaller than the corresponding ratios for the other lines of sight. The fact that the high-temperature [O I] 63 μm line, at an excitation temperature of about 228 K above ground, is not detected at all toward Ced 201, is consistent with these results if the gas tem-

TABLE 3
ISO OBSERVATIONS OF CED 201

Line (W m^{-2})	I	θ_{beam}
[C II] (158 μm)	3.80×10^{-15}	90"
[O I] (63 μm)	$< 8 \times 10^{-15}$	90"
H_2 S(1) (17 μm)	1.10×10^{-16}	14" × 27"
H_2 S(3) (9 μm)	5.61×10^{-17}	14" × 20"

perature is smaller than 150 K throughout most of the cloud (see the PDR models below).

3. A PHYSICAL MODEL FOR CED 201

The analysis of the data and construction of a physical model for Ced 201 will proceed in several steps. First, the average density, temperature, and abundances of observed species are determined from the observations through a simple excitation model. The chemical abundances are then reproduced through iteration of more elaborate one- and three-dimensional PDR models, which incorporate the chemical and thermal balance of the medium and the geometry of the reflection nebula. The motivation for the latter is that the spatial variations in the temperature and chemical abundances strongly influence the observed line intensities.

The intensities of emission lines are determined by the level populations and optical depth along the line of sight. A one-dimensional escape probability radiative transfer code has been applied to determine these quantities for the detected lines. The code includes collisional and radiative (de-) excitation processes and computes the level populations and line optical depth for a given set of physical parameters: density, temperature, column density, line width, and the temperature of the cosmic microwave background. Comparison with the observed intensities then results in a first guess for the beam-averaged kinetic temperature, density, and column density of the observed species. This radiative transfer code and the procedure for analyzing the data has been described by Jansen, van Dishoeck, & Black (1994) and Jansen (1995). In Table 4 the derived physical parameters are summarized. The kinetic temperature and the density of the main collision partner, molecular hydrogen, have been determined using the line intensities of the ^{12}CO and ^{13}CO transitions. The optically thick ^{12}CO lines were used to constrain the kinetic temperature, i.e., this is the temperature of the (self-shielding) molecular gas, whereas the ^{13}CO 3–2/2–1 line ratio was used as the main density probe (see Fig. 8a of Hogerheijde, Jansen, & van Dishoeck 1995).

It is important to realize that the C^+ column density is quite sensitive to the temperature structure of the cloud because of its excitation temperature of 92 K. For the one-dimensional and three-dimensional models we shall therefore compare with the observed flux directly. Since the more detailed models discussed below provide a good fit to the observed line strengths and indicate column densities quite similar (within the errors) to the one above, we will use this

knowledge and the value of the C^+ column density to derive now the gas-phase carbon abundance.

The gas-phase carbon budget is dominated by ^{12}CO , C, and C^+ . The sum of the derived column densities yields for the column density of gas-phase carbon $N(^{12}\text{C}) = (6 \pm 2) \times 10^{17} \text{ cm}^{-2}$. If it is assumed that the central gas cloud of Ced 201 is spherical, then one can compare the gas-phase carbon column density with the column density of hydrogen nuclei (N_{H}) along the line of sight. For spherical symmetry, $N_{\text{H}} = n_{\text{H}} \times \text{diameter} = (7.6 \pm 2.3) \times 10^{21} \text{ cm}^{-2}$, where the diameter from the ^{12}CO 2–1 map is 120" at 420 pc and the error is dominated by the noncircularity of the map. Thus, one finds for the gas-phase carbon abundance $A(\text{C}) = (7.9 \pm 3.5) \times 10^{-5}$. The cosmic abundance of carbon is $\approx 4 \times 10^{-4}$. Note here that the cosmic abundances are thought to be 30% lower than the solar abundances (cf. Meyer 1997). One finds for Ced 201 that the fraction of carbon in the gas phase is $20\% \pm 8\%$. For diffuse clouds a gas-phase carbon abundance of 1.4×10^{-4} is derived based on Goddard High Resolution Spectrograph/*Hubble Space Telescope* observations (Cardelli et al. 1993), consistent with the result found here.

If one assumes a carbon abundance of 10^{-4} , that C^+ is the dominant carbon-bearing species in the atomic PDR zone, and that the ambient density is above the critical density of $\sim 3 \times 10^3 \text{ cm}^{-3}$ (LTE) as motivated by the detected CO emission, then the size of the emitting region and the energy rate per hydrogen nucleus required to reproduce the observed line flux can be estimated. Clearly, various combinations of size and energy rate per H atom will yield identical line luminosities. Still, in LTE one cannot increase the emitted flux by a large amount unless the ambient temperature is below the excitation temperature, in which case the line would be quite weak. Therefore, taking a size of $\sim 120''$ from the CO and *IRAS* dust maps, one cannot make the [C II] emitting region much smaller than this without violating the observations, i.e., above 92 K per collision one increases mostly the ambient temperature and not the line luminosity. From these considerations it follows (to first order) that the beam filling factor of the emitting gas is roughly unity and the ambient temperature in the [C II] emitting region is not less than the excitation temperature of 92 K.

3.1. The One-dimensional PDR Model

Previous studies of PDRs illuminated by an (interstellar) radiation field with an effective temperature of about 30,000 K have been performed by Tielens & Hollenbach (1985), van Dishoeck & Black (1988), Burton, Hollenbach, & Tielens (1990), Hollenbach, Takahashi, & Tielens (1991), le Bourlot et al. (1992), and Störzer, Stutzki, & Sternberg (1996) at various levels of sophistication. Spaans et al. (1994) extended PDR calculations to softer ($T_{\text{eff}} = 20,000\text{--}6000 \text{ K}$) radiation fields in order to study the changes in the photoelectric heating efficiency. In this work two different models valid for clouds illuminated by an intense but soft radiation field, the one-dimensional PDR model and the three-dimensional PDR model, will be applied to, and tested for, Ced 201.

The one-dimensional PDR model is an extension of the diffuse cloud model of van Dishoeck & Black (1986) and is thoroughly described by Jansen et al. (1995, also referred to as the Leiden PDR model). In this model, the PDR is described as an infinite plane-parallel slab in thermal and

TABLE 4
PHYSICAL PARAMETERS AND COLUMN
DENSITIES OF CED 201

Parameter	Value
T	$(40 \pm 10) \text{ K}$
$n(\text{H}_2)$	$(5000 \pm 1000) \text{ cm}^{-3}$
$N(\text{CO})$	$(2 \pm 1) \times 10^{17} \text{ cm}^{-2}$
$N(^{13}\text{CO})$	$(3 \pm 1) \times 10^{15} \text{ cm}^{-2}$
$N(\text{CI})$	$< 2 \times 10^{16} \text{ cm}^{-2}$
$N(\text{C II})$	$(4 \pm 2) \times 10^{17} \text{ cm}^{-2}$
$N(\text{C}^{18}\text{O})$	$< 4 \times 10^{13} \text{ cm}^{-2}$
$N(\text{HCO}^+)$	$(8 \pm 3) \times 10^{11} \text{ cm}^{-2}$
$N(\text{CS})$	$< 1 \times 10^{12} \text{ cm}^{-2}$
$N(\text{O I})$	$< 4 \times 10^{18} \text{ cm}^{-2}$

chemical equilibrium with a radiation field incident from one side. The calculation of the chemical conditions in the PDR is performed in spatial steps, where the radiation field at a certain point is determined by calculating the attenuation by dust grains and optical depth effects in the UV absorption lines of H_2 and CO, which lead to dissociation. Moreover, shielding of CO by overlapping H_2 absorption lines (mutual shielding) is also taken into account (van Dishoeck & Black 1988). The chemical network includes 215 different species, based on 24 elements and the isotopes of H, C, and O (Jansen et al. 1995). The thermal balance is calculated simultaneously with the chemistry. The heating processes include photoelectric heating by dust grains and PAHs (Bakes & Tielens 1994), heating by cosmic rays ($\zeta = 5.0 \times 10^{-17} \text{ s}^{-1}$), H_2 formation heating, carbon photoionization heating, and collisional deexcitation of vibrationally excited H_2 (Tielens & Hollenbach 1985; Sternberg & Dalgarno 1989). Cooling is provided by spontaneous decay of collisionally excited fine-structure levels of C^+ , C, and O and rotational levels of CO.

3.2. The Three-dimensional PDR Model

In addition to the one-dimensional PDR model, the three-dimensional model developed by Spaans (1996), hereafter referred to as the 3D PDR model, is applied to Ced 201. Analogous to the one-dimensional PDR (1D PDR) model, this model calculates the thermal and chemical balance of the cool PDR, using the stellar radiation field, the morphology, the elemental abundances, and the (constant) density as input parameters. Nevertheless, differences between the models occur, due to the geometry, radiative transfer, and chemical network. The radiative transfer in the 3D PDR model is extended from one to three dimensions, thus enabling one to interpret the line intensities from geometrically more complex clouds and to take into account the position of the illuminating star. Furthermore, the interstellar radiation field (ISRF) (Draine 1978) is explicitly taken into account as an isotropic background radiation field illuminating the side of the cloud opposite to the star.

In contrast with the escape probability method of the 1D PDR model, the 3D PDR model uses Monte Carlo radiative transfer (Spaans & van Langevelde 1992; Spaans 1996). According to this method, the PDR is divided into a large number of different cells with a typical size no larger than the mean free path of a photon. The physical conditions differ in each cell, thus influencing the excitation of atomic and molecular lines. Calculation of the radiative transfer proceeds by determining the stimulated emission and absorption (line and continuum) for propagating photon packages in each cell simultaneously. Spontaneous emission of line photon packages occurs in random directions. The chemical network incorporated in the 3D PDR model is more limited and includes only the ~ 40 most important observable species. Nevertheless, the network is shown to be detailed enough to model the $C^+/C/CO$ transition accurately (Spaans & van Dishoeck 1997).

4. RESULTS

Since the central gas cloud and the illuminating star are located in the same direction, the abundances as a function of visual extinction, calculated by the models, can be directly converted into column densities by integrating over the total extent along the line of sight. The aim of the con-

structed models is to reproduce the observed column densities, in particular the gas-phase carbon column density $N(^{12}C)$, the $[C \text{ II}]$ and $[O \text{ I}]$ line intensities, and to determine the best-fit input parameters of the one- and three-dimensional models.

Table 5 summarizes the input parameters resulting in the best-fit 1D PDR model. The illuminating radiation field is determined by considering the central star as a blackbody with $T_{\text{eff}} = 10,000 \text{ K}$, placed at a distance of $R_{\text{nebula}} = 0.4 \text{ pc}$. This corresponds to a value of $G_0 = 200$ in units of the average interstellar radiation between 13.6 and 2 eV (Spaans et al. 1994), which is derived from the spectral type of the star and the infrared observations presented by Casey (1991) in a straightforward manner. The density of hydrogen nuclei in Ced 201 is found to be $n_H = 2n(H_2) + n(H) = 1.2 \times 10^4 \text{ cm}^{-3}$ and reproduces well the observed chemical abundances. The best-fit column density of molecular hydrogen $N(H_2) = 1.6 \times 10^{21} \text{ cm}^{-2}$ is a measure of the physical size of the cloud. When compared with the spherically symmetric case, $N(H_2)_{\text{sph. symm.}} = 3.8 \times 10^{21} \text{ cm}^{-2}$, its value indicates that the PDR is flattened along the line of sight. Note that this also implies that the abundance of gas-phase carbon must be higher than 20%. In fact, the flattened geometry yields 46% for the abundance of carbon in the gas phase relative to the cosmic abundance. This revised gas-phase abundance is thus a factor of 1.3 higher than the value of 1.4×10^{-4} found for diffuse clouds. The best-fit model also constrains the gas-phase abundances δ of several other elements, which are shown in Table 5. The gas-phase fraction of nitrogen is rather arbitrarily chosen, since no observations of nitrogen-bearing species were obtained.

The 3D PDR model is applied consistently with the 1D PDR model. That is, the only input parameter of the 3D PDR model that can be modified for a constant density cloud is the three-dimensional geometry of the cool PDR. The best reproductions of the observed column densities are obtained for an oblate ellipsoid with an axis ratio of 2.4. The one- and three-dimensional models that yield the best fit to the observations are presented in Table 6.

4.1. Chemical Structure

The 1D PDR model yields the abundances as functions of depth for approximately 200 species, of which the most important ones are plotted in Figure 2. The assumed isotope ratios are $[^{12}C]/[^{13}C] = 60$ and $[^{16}O]/[^{18}O] = 500$. At the illuminated side of Ced 201, ionized carbon is the dominant carbon-bearing species. Because of line shielding and attenuation by intervening dust, the ionized carbon is converted into neutral carbon and carbon

TABLE 5
INPUT PARAMETERS FOR THE BEST
FIT OF THE 1D PDR MODEL

Parameter	Value
R_{nebula}	0.4 pc
n_H	$1.2 \times 10^4 \text{ cm}^{-3}$
$N(H_2)$	$1.6 \times 10^{21} \text{ cm}^{-2}$
δC	0.80
δO	0.80
δS	0.01
δN	0.70
δmetals	0.02

TABLE 6
COMPARISON BETWEEN THE OBSERVED COLUMN DENSITIES, THE 1D PDR MODEL,
AND THE 3D PDR MODEL (IN UNITS OF cm^{-2})

Species	Observed	1D PDR	3D PDR Model
H_2	-	1.6×10^{21}	1.5×10^{21}
^{12}CO	$(2 \pm 1) \times 10^{17}$	2.3×10^{17}	2.1×10^{17}
^{13}CO	$(3 \pm 1) \times 10^{15}$	4.4×10^{15}	3.1×10^{15}
C^{18}O	$< 4 \times 10^{13}$	7.2×10^{13}	3.1×10^{13}
C	$< 2 \times 10^{16}$	5.2×10^{16}	3.2×10^{16}
C^+	$(4 \pm 2) \times 10^{17}$	3.2×10^{17}	3.7×10^{17}
CS	$< 1 \times 10^{12}$	6.3×10^{11}	5.1×10^{11}
HCO^+	$(8 \pm 3) \times 10^{11}$	4.1×10^{11}	6.8×10^{11}

monoxide at $A_V \sim 1$ mag (Tielens & Hollenbach 1985; Black & van Dishoeck 1987 and references therein). Nowhere in the cloud does neutral carbon become the dominant carbon-bearing species.

The abundances of several species determined by the 3D PDR model are shown in Figure 3. Consistent with the 1D PDR model, the $\text{C}^+/\text{C}/\text{CO}$ transition occurs at an extinction of $A_V \sim 1$ mag. Because of the ISRF, which illuminates the cloud from all directions, a second $\text{C}^+/\text{C}/\text{CO}$ transition zone is present at $A_V \sim 2$ mag on the far side of the PDR. Atomic hydrogen is the dominant form of hydrogen at the

illuminated edge, but the shielding of H_2 is very efficient and leads to a sharp transition.

4.2. Thermal Balance and Small Grains

Both the 3D PDR model and the 1D PDR model compute the thermal balance in Ced 201. Figures 4 and 5 show the heating and cooling rates as functions of depth determined by the 1D PDR model. Except for the heating

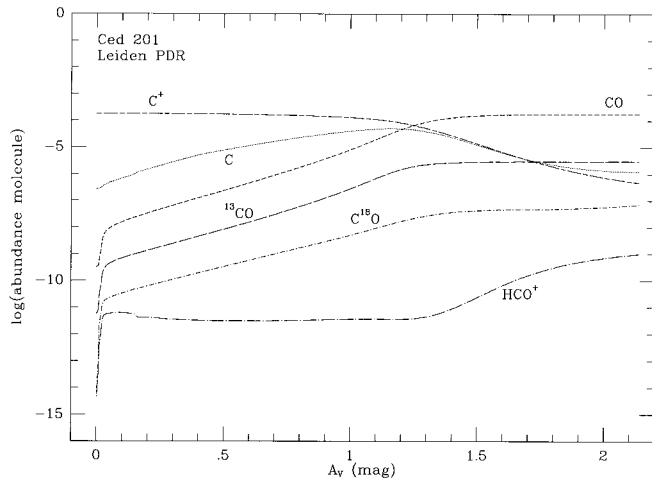


FIG. 2.—Abundances of carbon-bearing species in Ced 201 as functions of visual extinction into the cloud, for the 1D PDR model.

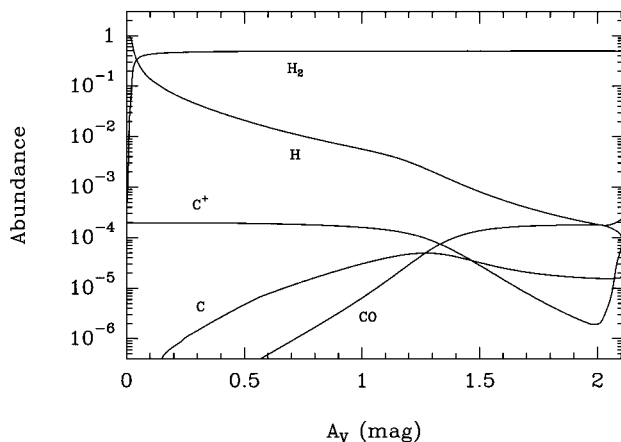


FIG. 3.—Abundances of several species as functions of visual extinction, for the three-dimensional model.

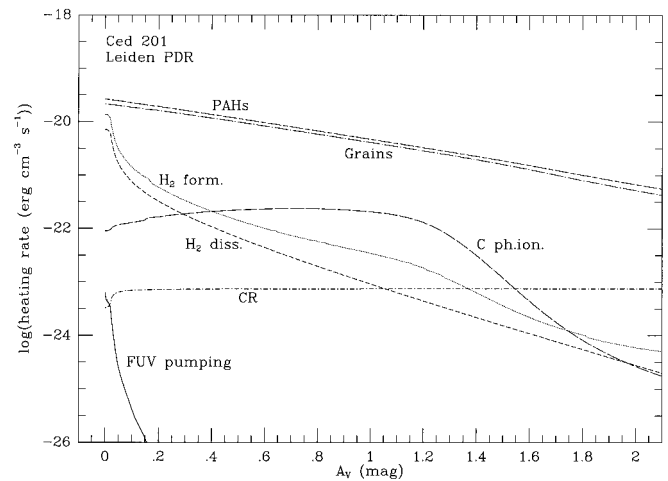


FIG. 4.—Most important heating rates as functions of visual extinction (1D PDR model).

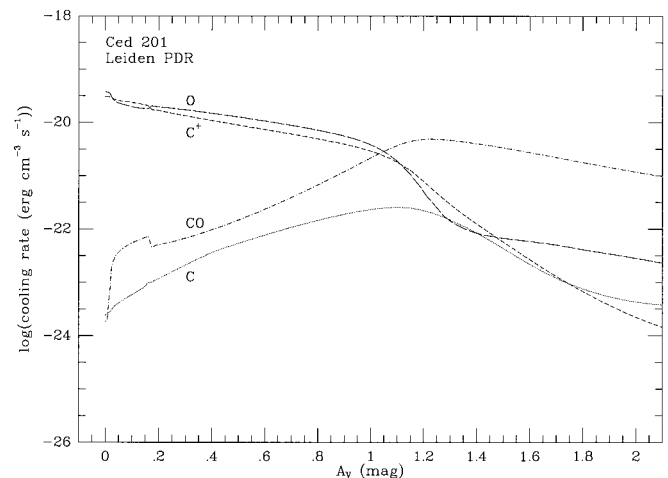


FIG. 5.—Cooling rates originating from the main coolants as functions of visual extinction (1D PDR model).

by cosmic rays, all heating mechanisms decrease with depth into the cloud. Photoelectric emissions by PAHs and dust grains are the dominant heating mechanisms in Ced 201. The heating rates of these two processes are equal, although only 10% of the solid state carbon is incorporated into PAHs in the best-fit model. This shows how quantum effects in PAHs can contribute significantly to the heating process in cool radiation fields (Bakes & Tielens 1994). Cooling is provided by radiative decay of collisionally excited species. The cooling rates due to the main coolants are shown in Figure 5 and depend strongly on the abundances of these species. The observations do not provide good constraints on the column density of atomic oxygen, and a gas-phase fraction of 3.2×10^{-4} is therefore assumed (Meyer 1997).

The thermal balance is established at an equilibrium temperature profile determined by the heating and cooling rates. Figures 6 and 7 show these profiles for the 1D PDR model and the 3D PDR model, respectively. The temperature profiles calculated by both models are approximately the same. The temperature at the illuminated edge is 168 K according to the 3D PDR model and 169 K for the 1D PDR model. The temperature decreases with increasing depth and is for both models ~ 40 K at $A_V = 1$ mag, where the temperature tracer carbon monoxide becomes abundant. According to the 1D PDR model, the temperature gradually declines at the dark side of the PDR. Because of the ISRF, however, the 3D PDR model predicts that the temperature will increase again, after reaching its minimum of 22 K at $A_V = 1.8$ mag, and become 34 K at the dark side of Ced 201.

For the best-fit models to the chemical abundances, one can determine the model-dependent, i.e., with the distance to the star fixed by the infrared observations, contribution to the heating rate from PAHs and VSGs. The models indicate that 10% of the gas-phase carbon is locked up in the form of PAHs, i.e., $D_{\text{PAH}} = 0.1$, where PAHs are defined as any carbonaceous particle of linear size less than 15 Å. Additional models were run without any contribution of PAHs and VSGs to check the robustness of this result. The resulting thermal balance in the latter case yields temperatures at the edge of the cloud that are lower by 50% and strongly underestimates the observed [C II] flux. The fraction $D_{\text{PAH}} = 0.1$ also yields good agreement with the

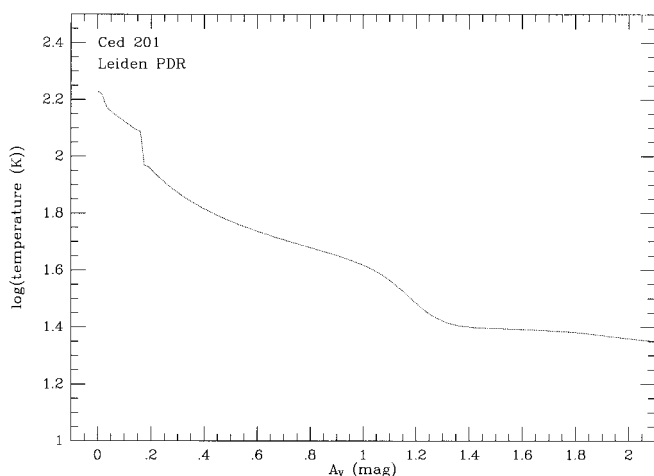


FIG. 6.—Temperature distribution throughout the cloud, according to the 1D PDR model.

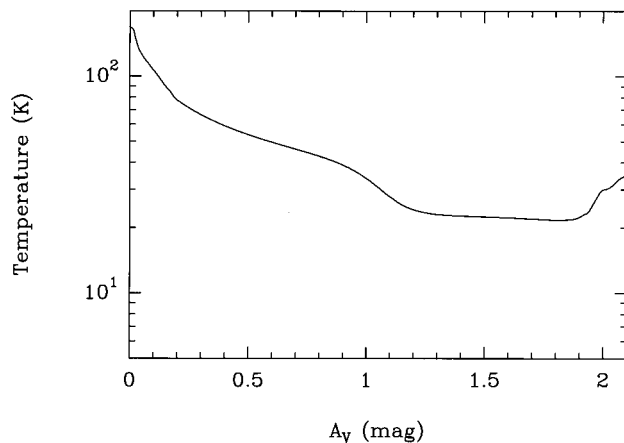


FIG. 7.—Kinetic gas temperature as a function of extinction, according to the 3D PDR model.

observed CO excitation temperatures. The precise value for D_{PAH} depends on the model. Nevertheless, a firm conclusion is that heating by PAHs and VSGs is required to explain the observed properties of Ced 201, provided no heating sources other than photoelectric heating and cosmic rays are important.

A final crucial comparison comes from the predicted [C II] 158 μm and [O I] 63 μm line intensities, because they reflect the thermal balance of the medium most strongly. In the one-dimensional case one finds values of 1.1×10^{-5} for [C II] and 1.9×10^{-5} ergs $\text{s}^{-1} \text{cm}^{-2} \text{sr}^{-1}$ for [O I]. The three-dimensional results are systematically higher and yield 1.8×10^{-5} and 2.7×10^{-5} ergs $\text{s}^{-1} \text{cm}^{-2} \text{sr}^{-1}$, respectively. Comparison with the observed [C II] intensity would thus favor the three-dimensional model, but the difference is small.

4.3. Pure Rotational H_2 Lines

The H_2 $J = 3$ and $J = 5$ levels in the vibrational ground state lie at ~ 1000 and ~ 2500 K above ground and therefore trace warm molecular gas. The ISO observations of the H_2 S(1) and S(3) pure rotational transitions are not included in the PDR models, since at kinetic temperatures of $T < 100$ K, i.e., in a large part of Ced 201, the absolute intensities of these lines are negligible. For higher temperatures these lines are useful temperature tracers because they are optically thin and the level populations are in thermal equilibrium. The ratio between the observed transitions is $I(9 \mu\text{m})/I(17 \mu\text{m}) = 0.69$, which indicates a kinetic temperature of $T \sim 330$ K (Black & van Dishoeck 1987).

This observational result is clearly at variance with the model predictions, particularly since the effective temperature of the illuminating is low. It appears that an additional heating source is required in some part of the cloud. If we assume that a thin layer of hot gas is present at the illuminated edge or anywhere else inside the cool PDR, then it follows from the absolute intensities that this layer is not thicker than $\delta A_V \sim 0.05$ mag for a mean H_2 fraction of 0.2. We therefore feel that the value of D_{PAH} remains secure since the chemical constraints that enter into it derive from regions in the cloud with $A_V > 0.3$ mag. The upper limit of 5×10^{-5} ergs $\text{s}^{-1} \text{cm}^{-2} \text{sr}^{-1}$ for the [O I] 63 μm line and its density dependence of $1.0 \times 10^{-8} n_{\text{H}_2}$ ergs $\text{s}^{-1} \text{cm}^{-2} \text{sr}^{-1}$ for temperatures higher than 228 K and subthermal excitation indicate that an upper limit for the H_2 gas density is

$5 \times 10^3 \text{ cm}^{-3}$ when a unity beam filling factor is adopted. From the CO maps we estimate a beam dilution factor of not more than 2, so the upper limit is consistent with the CO density estimate and vibrational deexcitation heating by H_2 can be ruled out.

Furthermore, the continuum intensity observed by *IRAS* is around $2 \times 10^{-3} \text{ ergs s}^{-1} \text{ cm}^{-2} \text{ sr}^{-1}$, whereas the $[\text{C II}]$ intensity is $2 \times 10^{-5} \text{ ergs s}^{-1} \text{ cm}^{-2} \text{ sr}^{-1}$. This translates into a heating efficiency for the gas of 1%, a generic value for PDRs. The temperature of 300 K itself requires a G_0 of 5×10^3 for an ambient H_2 density of $5 \times 10^3 \text{ cm}^{-3}$, incompatible with the value $G_0 = 200$ from the illuminating star. All in all, the high-temperature molecular gas remains to be explained and does not seem to be accommodated by the process of photoelectric heating. In fact, observations presented by Witt et al. (1987) on the scattering properties of dust in Ced 201 indicate that there is a narrow size distribution of grains skewed toward larger than average particle sizes. This renders a larger contribution to the photoelectric heating by small grains unlikely.

One might argue that the H_2 levels are populated through UV pumping. Even though the reflection nebula is relatively close to the illuminating star, the low effective stellar temperature strongly quenches the 912–1110 Å flux relative for H_2 fluorescence. A straightforward calculation shows that UV irradiation can account for at most 20% of the S(3) line, thereby rendering it a minor contribution.

An additional heating source like turbulent dissipation could be present in the cool PDR (Falgarone & Puget 1995). This requires the input of kinetic energy on the scale of the cloud, possibly through a weak (3–5 km s^{-1}) shock. A C-shock of 7 km s^{-1} into a gas of preshock density 10^4 cm^{-3} would also suffice but would likely lead to an observ-

able $[\text{O I}]$ 63 μm line. Finally, the case of Ced 201 appears not to be unique. Observations obtained by Timmermann et al. (1996) for S140 indicate similarly warm gas. It would be quite interesting if more of such warm regions show up in H_2 rotational line data.

5. CONCLUSIONS

The 1D PDR and the 3D PDR model reproduce the chemical abundances and the thermal balance of the cool PDR Ced 201 as derived from the observations. All observed lines, obtained with the JCMT, *ISO*, and NRAO, are accommodated by these models, except for the pure rotational transitions of H_2 . The observed H_2 S(1) and S(3) line intensities indicate the presence of hot gas with a kinetic temperature of $T \sim 330 \text{ K}$, which is probably located in a thin layer of $\delta A_V \sim 0.05 \text{ mag}$ at the illuminated edge of the cool PDR. The best-fit models indicate that the gas-phase carbon abundance is 50% of solar and that 10% of the available carbon atoms is in the form of PAHs and VSGs.

Research in astrochemistry in Leiden is supported by the Netherlands Organization for Scientific Research. M. S. is supported by NASA through grant HF-01101.01-97A, awarded by the Space Telescope Institute, which is operated by the Association of Universities for Research in Astronomy, Inc., for NASA under contract NAS 5-26555. We are grateful for the assistance of Jante Salverda and Remo Tilanus in obtaining the observations presented in this work. We would like to thank Wing-Fai Thi for the *ISO*-SWS reduction, Byron Mattingly for obtaining the NRAO 12 m observations, and John Black for general discussions and computer codes.

REFERENCES

- Bakes, E. L. O., & Tielens, A. G. G. M. 1994, *ApJ*, 427, 822
 Black, J. H., & van Dishoeck, E. F. 1987, *ApJ*, 322, 412
 Boreiko, R. T., Betz, A. L., & Zmuidzinas, J. 1990, *ApJ*, 353, 181
 Burton, M. G., Hollenbach, D. J., & Tielens, A. G. G. M. 1990, *ApJ*, 365, 620
 Cardelli, J. A., Federman, S. R., Lambert, D. L., & Theodosiou, C. E. 1993, *ApJ*, 416, L41
 Casey, S. C. 1991, *ApJ*, 371, 183
 Clegg, P. E., et al. 1996, *A&A*, 315, L38
 de Graauw, T., et al. 1996, *A&A*, 315, L345
 Draine, B. T. 1978, *ApJS*, 36, 595
 Falgarone, E., & Puget, J.-L. 1995, *A&A*, 293, 840
 Hogerheijde, M. R., Jansen, D. J., & van Dishoeck, E. F. 1995, *A&A*, 294, 792
 Hollenbach, D. J., Takahashi, T., & Tielens, A. G. G. M. 1991, *ApJ*, 377, 192
 Hollenbach, D. J., & Tielens, A. G. G. M. 1997, *Ann. Rev. Astron. Astrophys.*, 35, 179
 Jansen, D. J. 1995, Ph.D. thesis, Leiden Obs.
 Jansen, D. J., van Dishoeck, E. F., & Black, J. H. 1994, *A&A*, 282, 605
 Jansen, D. J., van Dishoeck, E. F., Black, J. H., Spaans, M., & Sosin, C. 1995, *A&A*, 302, 223
 le Bourlot, J., Pineau de Forêts, G., Roueff, E., & Flower, D. R. 1992, *A&A*, 267, 233
 Meyer, D. M. 1997, in *IAU Symp. 178, Molecules in Astrophysics: Probes and Processes*, ed. E. F. van Dishoeck (Dordrecht: Kluwer), 407
 Minchin, N. R., White, G. J., Stutzki, J., & Krause, D. 1994, *A&A*, 291, 250
 Spaans, M. 1996, *A&A*, 307, 271
 Spaans, M., Tielens, A. G. G. M., van Dishoeck, E. F., & Bakes, E. L. O. 1994, *ApJ*, 437, 270
 Spaans, M., & van Dishoeck, E. F. 1997, *A&A*, 323, 953
 Spaans, M., & van Langevelde, H. J. 1992, *MNRAS*, 258, 159
 Sternberg, A., & Dalgarno, A. 1989, *ApJ*, 338, 197
 Störzer, H., Stutzki, J., & Sternberg, A. 1996, *A&A*, 310, 592
 Tielens, A. G. G. M., & Hollenbach, D. J. 1985, *ApJ*, 291, 722
 Timmermann, R., Bertoldi, F., Wright, C. M., Drapatz, S., Draine, B. T., Haser, L., & Sternberg, A. 1996, *A&A*, 315, L281
 van Dishoeck, E. F., & Black, J. H. 1986, *ApJS*, 62, 109
 ———. 1988, *ApJ*, 334, 771
 Witt, A. V., Graff, S. M., Bohlin, R. C., & Stecher, T. P. 1987, *ApJ*, 321, 912